

Dynamics Computation of Soft-Rigid Hybrid-Link System and Its Application to Motion Analysis of an Athlete Wearing Sport Prosthesis

Sunghee Kim^a, Yuta Shimane^a, Taiki Ishigaki^b, and Ko Yamamoto^a

^aDepartment of Mechano-Informatics, University of Tokyo, 7-3-1 Hongo, Bunkyo-Ku, Tokyo, Japan ; ^bResearch Institute for Science and Technology, Tokyo University of Science, Katsushika-ku, Tokyo, Japan

ARTICLE HISTORY

Compiled May 14, 2026

ABSTRACT

This paper presents a motion analysis framework for an athlete wearing sport-specific flexible prosthesis based on the soft-rigid hybrid-link system. Such a motion analysis is a challenging problem because we need to consider the interaction force between the rigid human skeleton system and a flexible prosthesis. However, most of human musculoskeletal models are based on the computation framework of a rigid-body multi-link system. Recently in soft robotics research field, fast and efficient modeling methods were developed for a flexible rod deformation, which allows us to build a hybrid-link system that integrates rigid-link and soft-bodies in a unified formulation. We apply inverse kinematics of the hybrid-link system to motion reconstruction from a motion captured data, and also present the estimation of the joint torques and ground reaction force by inverse dynamics. Through a human subject experiment, we show that the inverse dynamics achieved approximately 12% error on the ground reaction force estimation. Furthermore, we provide the muscle force estimation considering muscle amputation and interaction force with the prosthesis leg deformation.

KEYWORDS

Kinematics and Dynamics; Biomechanics; Soft robotics

1. Introduction

A prosthesis leg specialized for sports opens the door for individuals with congenital or acquired limb disabilities to enjoy sports and participate in competitions such as the Paralympics [1]. As the developments in robotics and biomechanics, motion analysis based on a human musculo-skeletal model [2,3] will provide a quantitative knowledge on performance analysis, training, and injury prevention not only for able-bodied athlete but also for Para-athlete. However, motion analysis of an athlete wearing a flexible prosthesis is a challenging problem because we need to consider the interaction force between the rigid human skeleton system and a flexible prosthesis. Most of human musculoskeletal models are based on kinematics and dynamics computation framework of

CONTACT Ko Yamamoto. Email: yamamoto.ko@nsl.t.u-tokyo.ac.jp. This is an original manuscript of an article published by Taylor & Francis in *Advanced Robotics*, Vol.40, No.4, 2026 on 12 Jan 2026, available online: <https://doi.org/10.1080/01691864.2025.2611426>.

a rigid-body multi-link system and cannot directly deal with a continuous deformation of a leaf-spring prosthesis leg. Previous studies employed a rigid-body model [4] or simple spring-damper models [5,6] for a prosthesis sprinting motion. These models were too simple to appropriately model the deformation of a prosthesis.

The field of soft robotics has explored various methods for modeling flexible deformation. The finite element method (FEM) is a representative technique to calculate a continuous deformation of a soft structure [7–10]. However, one of the known limitations in FEM is its high computational cost [11,12], especially in the case that a complicated shape is divided into a lot of meshes. While FEM is suitable for an object with complicated shape, there are methods specific for a rod or beam structure based on the Cosserat rod theory [13], which can offer much faster computation and is suitable for a leaf-spring prosthesis. This theory conceptualizes a rod as a deformable vector with an orientation, allowing each point along its central axis coordinate to be described using a local frame. Thanks to this characteristic, the analysis of a soft continuum based on the Cosserat rod theory shows a framework similar to that of the rigid-body multi-link system. In particular, the Piecewise Constant Strain (PCS) model [14], [15] is compatible with the rigid-body multi-link system because it discretizes a flexible rod or beam structure into a finite number of segments and assumes a constant strain in each segment. Because of its compatibility, some studies have proposed hybrid-link models that integrated rigid-links and soft-bodies [16,17].

In this study, we apply the framework of kinematics and dynamics computation of a hybrid-link system to dynamic motion analysis of an athlete wearing a sports-specific prosthesis. Fig. 1 provides an overview of the motion analysis framework, including inverse kinematics (IK) calculation for the motion capture measurement, inverse dynamics (ID) calculation for the estimation of joint torques and ground reaction forces, and muscle-force optimization considering the interaction force between the human-body and prosthesis. Through a human subject experiment, we validate that dynamics computation based on the hybrid-link can provide a good estimation of the ground reaction force. Moreover, we demonstrate a visualization of the muscle-force optimization result during the motion.

The rest of this paper is organized as follows. Section 2 describes the basic formulations of the PCS model and the hybrid-link system, and presents the inverse kinematics of the hybrid-link system for a motion capture measurement. Then, the inverse dynamics of the hybrid-link system for the estimation of the ground reaction force, and muscle force optimization are introduced. Section 3 reports experimental results including motion capture measurement, ground force estimation by inverse dynamics, and a visualization of the muscle force estimation, providing a preliminary result on the muscle force estimation. Finally, Section 4 provides discussions on the experimental results, and Section 5 summarizes the obtained results and concludes the paper.

A part of this paper was reported in our previous conference paper [18]. This study provides more dynamical analyses using inverse dynamics and muscle-force optimization whereas [18] reported a simple analysis of the inverse kinematics for the motion capture measurement, mainly presented in Section 3.1.

Ethics approval for the experimental procedures in this study was granted by the Human Research Committee at Graduation School of Information Science and Technology, the University of Tokyo (approval no.: UT-IST-RE-220209). Hereafter, we use the following basic notations and definitions.

- \mathbf{E} and \mathbf{O} denote the unit and zero matrices, respectively.

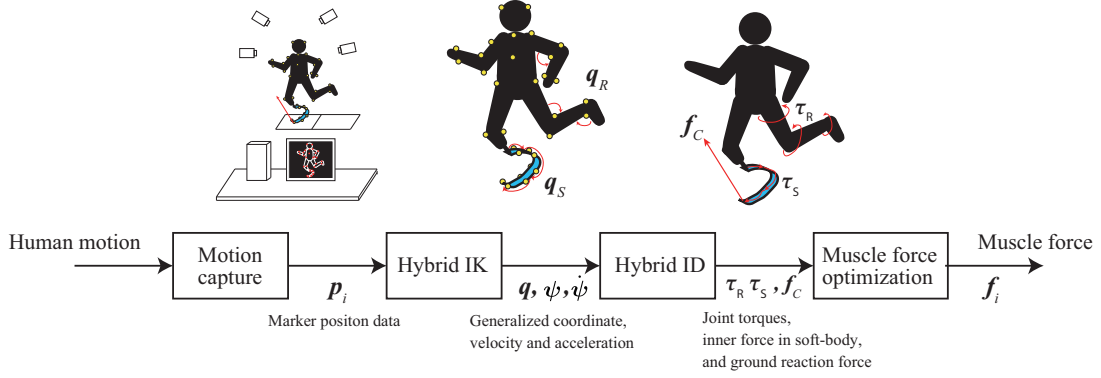


Figure 1. Overview for the motion analysis framework based on the hybrid-link system. From a motion capture system, we reconstruct human motion and prosthesis deformation by inverse kinematics. Then, inverse dynamics calculates the joint torques, inner force in the prosthesis and the ground reaction force. From the obtained joint torques and interaction force from the prosthesis, we estimate muscle tendon forces by an optimization.

- $SO(3)$ is the three dimensional special orthogonal group, and $so(3)$ is its Lie algebra.
- $SE(3)$ is the three dimensional special Euclid group, and $se(3)$ is its Lie algebra.
- Given a vector $\mathbf{a} = [a_1 \ a_2 \ a_3]^T \in \mathbb{R}^3$, the skew-symmetric matrix $[\mathbf{a} \times]$ is defined as

$$[\mathbf{a} \times] := \begin{bmatrix} 0 & -a_3 & a_2 \\ a_3 & 0 & -a_1 \\ -a_2 & a_1 & 0 \end{bmatrix} \in so(3). \quad (1)$$

- Given three-dimensional vectors \mathbf{a} and \mathbf{b} , and a six-dimensional vector $\mathbf{c} = [\mathbf{a}^T \ \mathbf{b}^T]^T$, operators $[\mathbf{c} \times]$ and $[\mathbf{c} \bullet]$ are defined as

$$[\mathbf{c} \times] := \begin{bmatrix} [\mathbf{a} \times] & \mathbf{b} \\ \mathbf{0}^T & 0 \end{bmatrix} \in se(3), \quad (2)$$

$$[\mathbf{c} \bullet] := \begin{bmatrix} [\mathbf{a} \times] & \mathbf{O} \\ [\mathbf{b} \times] & [\mathbf{a} \times] \end{bmatrix}. \quad (3)$$

- $\|\mathbf{x}\|_{\mathbf{W}}^2 = \mathbf{x}^T \mathbf{W} \mathbf{x}$ is a weighted squared norm of a vector \mathbf{x} with a weighting matrix \mathbf{W} .

2. Methods

2.1. PCS Model

2.1.1. Kinematics of PCS Model

In Cosserat rod theory, the microsolid of a soft continuum along the central axis coordinate $s \in \mathbb{R}$ at a certain time $t \in \mathbb{R}$ is represented by a configuration curve

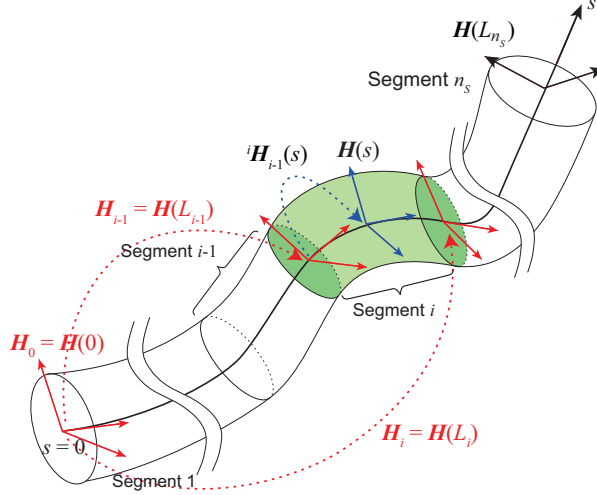


Figure 2. Schematic view of the PCS model

$\mathbf{H}(s, t) \in SE(3)$ as

$$\mathbf{H}(s, t) = \begin{bmatrix} \mathbf{R}(s, t) & \mathbf{p}(s, t) \\ \mathbf{0}^T & 1 \end{bmatrix} \quad (4)$$

where $\mathbf{R}(s, t) \in SO(3)$ is the rotational matrix and $\mathbf{p}(s, t) \in \mathbb{R}^3$ is the position vector. Hereinafter, t or s is omitted for simplicity when its meaning is obvious. Given the configuration curve $\mathbf{H}(s)$, a six-dimensional displacement $\boldsymbol{\xi}(s) \in \mathbb{R}^6$ is defined with the operator $[\boldsymbol{\xi}(s) \times]$ as

$$[\boldsymbol{\xi}(s) \times] := \mathbf{H}(s)^{-1} \frac{\partial \mathbf{H}}{\partial s}. \quad (5)$$

In this paper, we refer to the continuous deformation defined by Eq. (5) as *strain* although it is not exactly same with the strict definition in material mechanics.

Fig. 2 shows a schematic view of the PCS model [14], in which a rod is divided into a finite number of segments. Let n_s denote the number of segments, and define $L_{i-1} \leq s \leq L_i$ as segment i ($i = 1, \dots, n_s$) with $L_0 = 0$. The PCS model assumes that each segment has a constant strain $\boldsymbol{\xi}_i$, i.e.,

$$\boldsymbol{\xi}_i := \boldsymbol{\xi}(s) \quad (L_{i-1} \leq s \leq L_i). \quad (6)$$

Substituting Eq. (6) into Eq. (5), we obtain a first-order differential equation of $\mathbf{H}(s)$ as

$$\frac{\partial \mathbf{H}}{\partial s} = \mathbf{H}(s) [\boldsymbol{\xi}_i \times]. \quad (7)$$

From the solution of this equation, we can calculate the configuration curve in segment i as

$$\mathbf{H}_i(s) = \mathbf{H}(L_{i-1}) \exp\{(s - L_{i-1}) [\boldsymbol{\xi}_i \times]\}. \quad (8)$$

Note that we add the index i in the right-lower of $\mathbf{H}(s)$ to emphasize that this equation is satisfied in segment i . Then, we define

$$\mathbf{H}_{i-1} := \mathbf{H}(L_{i-1}), \text{ and} \quad (9)$$

$${}^{i-1}\mathbf{H}_i(s, \boldsymbol{\xi}_i) := \exp\{(s - L_{i-1})[\boldsymbol{\xi}_i \times]\}, \quad (10)$$

Eq. (8) can be rewritten as

$$\mathbf{H}_i(s) = \mathbf{H}_{i-1} {}^{i-1}\mathbf{H}_i(s, \boldsymbol{\xi}_i). \quad (11)$$

Moreover, using a notation of

$$\mathbf{H}_i = \mathbf{H}_i(L_i), \text{ and } {}^{i-1}\mathbf{H}_i(L_i, \boldsymbol{\xi}_i) = {}^{i-1}\mathbf{H}_i(\boldsymbol{\xi}_i) \quad (12)$$

we can obtain the following recursion that is similar to the traditional rigid-link system.

$$\mathbf{H}_i = \mathbf{H}_{i-1} {}^{i-1}\mathbf{H}_i(\boldsymbol{\xi}_i). \quad (13)$$

Given $\boldsymbol{\xi}_i$ of all segments, we can calculate the configuration curve at any coordinate by recursively applying Eq. (11) or Eq. (13). While Eq. (11) represents the forward kinematics inside segment i , Eq. (13) represents that for the beginning to the end of segment i . Therefore, we can define the generalized coordinate of the PCS model as

$$\mathbf{q}_s = [\boldsymbol{\xi}_1^T \quad \cdots \quad \boldsymbol{\xi}_{n_s}^T]^T \in \mathbb{R}^{6n_s}. \quad (14)$$

If the base of segment 1 ($s = 0$) is not fixed to the environment, we can add \mathbf{H}_0 in the generalized coordinate \mathbf{q}_s .

In Eq. (5), replacing s with t yields the definition of the spatial velocity [19] $\boldsymbol{\eta}(s)$ as

$$[\boldsymbol{\eta}(s) \times] := \mathbf{H}(s)^{-1} \frac{\partial \mathbf{H}}{\partial t} \quad (15)$$

Let $\boldsymbol{\eta}_i(s)$ denote the spatial velocity at the coordinate s in segment i . From the definition of $\boldsymbol{\eta}_i(s)$ and $\boldsymbol{\xi}(s)$, the following differential equation can be derived:

$$\frac{\partial \boldsymbol{\eta}_i}{\partial s} = \dot{\boldsymbol{\xi}}_i - [\boldsymbol{\xi}_i \bullet] \boldsymbol{\eta}(s). \quad (16)$$

The solution of Eq. (16) is obtained as follows:

$$\boldsymbol{\eta}_i(s) = {}^i\mathbf{A}(s)^{-1} \{ \boldsymbol{\eta}(L_{i-1}) + {}^i\mathbf{T}(s) \dot{\boldsymbol{\xi}}_i \}, \quad (17)$$

$${}^i\mathbf{A}(s) := \exp\{(s - L_{i-1})[\boldsymbol{\xi}_i \bullet]\}, \quad (18)$$

$${}^i\mathbf{T}(s) := \int_{L_{i-1}}^s \exp\{(x - L_{i-1})[\boldsymbol{\xi}_i \bullet]\} dx. \quad (19)$$

The recursive formula Eq. (17) represents differential kinematics of the PCS model. Therefore, we can obtain the relationship between $\boldsymbol{\eta}_i(s)$ and $\dot{\mathbf{q}}_s$ as follows:

$$\boldsymbol{\eta}_i(s) = \mathbf{J}_i(s) \dot{\mathbf{q}}_s, \quad (20)$$

where $\mathbf{J}_i(s) \in \mathbb{R}^{6 \times 6n_s}$ is the Jacobian matrix at s in segment i .

2.1.2. Dynamics of PCS Model

The dynamics of the continuous Cosserat rod with respect to the microsolid frame can be represented as

$$\mathbf{M}(s)\dot{\boldsymbol{\eta}} - [\boldsymbol{\eta}_\bullet]^T \mathbf{M}\boldsymbol{\eta} = \mathcal{F} \quad (21)$$

where $\mathbf{M}(s) \in \mathbb{R}^{6 \times 6}$ is a screw inertia matrix at s , and $\mathcal{F} \in \mathbb{R}^6$ is the force applied to the microsolid. From this equation, the dynamics of the PCS model is derived as follows [14]:

$$\mathbf{M}_s(\mathbf{q}_s)\ddot{\mathbf{q}}_s + \mathbf{C}(\mathbf{q}_s, \dot{\mathbf{q}}_s)\dot{\mathbf{q}}_s = \boldsymbol{\tau}_s \quad (22)$$

where

$$\mathbf{M}_s(\mathbf{q}_s) = \int_0^{L_n} \mathbf{J}^T \mathbf{M} \mathbf{J} ds, \quad (23)$$

$$\mathbf{C}_s(\mathbf{q}_s, \dot{\mathbf{q}}_s) = \int_0^{L_n} \left(\mathbf{J}^T \mathbf{M} \dot{\mathbf{J}} - \mathbf{J}^T [(\mathbf{J}\dot{\mathbf{q}})_\bullet]^T \mathbf{M} \mathbf{J} \right) ds, \quad (24)$$

$$\boldsymbol{\tau}_s = \int_0^{L_n} \mathbf{J}^T \mathcal{F} ds. \quad (25)$$

Especially in the case that only passive internal force applies inside the rod, $\boldsymbol{\tau}_s$ is given by

$$\boldsymbol{\tau}_s = \mathbf{K}_s(\mathbf{q}_{s,0} - \mathbf{q}_s) - \mathbf{D}_s \dot{\mathbf{q}}_s \quad (26)$$

where \mathbf{K}_s and $\mathbf{D}_s \in \mathbb{R}^{6n_s \times 6n_s}$ are stiffness and viscosity matrices, respectively. $\mathbf{q}_{s,0}$ is a neutral strain value in which no internal force is applied.

Because the structure of Eq. (22) is similar to that of the traditional rigid-link system, we can easily integrate the PCS model with rigid-link system as a hybrid-link system.

2.2. Structure of Hybrid-link System

Fig. 3 shows a conceptual illustration of a hybrid-link system that consists of rigid-links and soft-segments represented by the PCS model. As a general model, we consider that the base-link is not fixed to the environment, and that there are multiple contacts where $\mathbf{f}_{C,i}$ denotes a contact force. Without loss of generality, we can define the generalized coordinate vector \mathbf{q}_R that consists of the joint displacements of rigid-links, and \mathbf{q}_S that consists of the strains of all soft-segments, no matter the order of these connections. Note that \mathbf{q}_R is an N_R dimensional vector if we assume that each joint connecting rigid links is 1-DOF revolute or prismatic one, where N_R is the number of joints.

Then, we define the generalized coordinate of the hybrid-link system, \mathbf{q} , and the

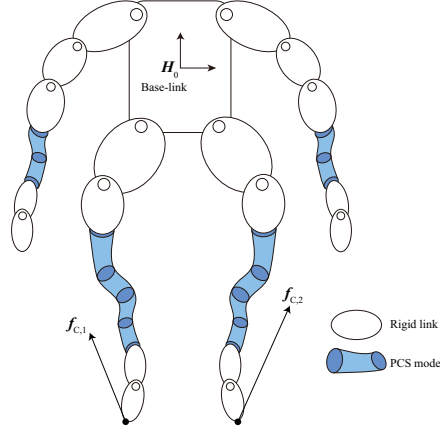


Figure 3. Conceptual illustration of a hybrid-link system that consists of rigid-links and soft-segments represented by the PCS model. We consider that the base-link is not fixed to the environment and that there are multiple contacts where $\mathbf{f}_{C,i}$ denote a contact force.

generalized velocity vector $\boldsymbol{\psi}$ as follows:

$$\mathbf{q} := \left\{ \mathbf{H}_0, [\mathbf{q}_R^T \quad \mathbf{q}_S^T]^T \right\}, \text{ and} \quad (27)$$

$$\boldsymbol{\psi} = [\boldsymbol{\eta}_0^T \quad \dot{\mathbf{q}}_R^T \quad \dot{\mathbf{q}}_S^T]^T \quad (28)$$

Note that we use the notation $\boldsymbol{\psi}$ for the generalized velocity, not $\dot{\mathbf{q}}$, because it is not directly obtained as the time-differential of \mathbf{q} .

The equation of motion of the hybrid-link system can be represented as follows:

$$\mathbf{M}(\mathbf{q})\dot{\boldsymbol{\psi}} + \mathbf{b}(\mathbf{q}, \boldsymbol{\psi}) = \boldsymbol{\tau} + \sum_i \mathbf{J}_{C,i}^T \mathbf{f}_{C,i}. \quad (29)$$

$$\mathbf{M}(\mathbf{q}) = \begin{bmatrix} \mathbf{M}_0 & \mathbf{M}_{0R} & \mathbf{M}_{0S} \\ \mathbf{M}_{0R}^T & \mathbf{M}_R & \mathbf{M}_{RS} \\ \mathbf{M}_{0S}^T & \mathbf{M}_{RS}^T & \mathbf{M}_S \end{bmatrix}, \quad \mathbf{b}(\mathbf{q}, \dot{\mathbf{q}}) = \begin{bmatrix} \mathbf{b}_0 \\ \mathbf{b}_R \\ \mathbf{b}_S \end{bmatrix}, \quad \boldsymbol{\tau} = \begin{bmatrix} \mathbf{0} \\ \boldsymbol{\tau}_R \\ \boldsymbol{\tau}_S \end{bmatrix}, \quad (30)$$

where $\mathbf{M}(\mathbf{q})$ is the inertia matrix, $\mathbf{b}(\mathbf{q}, \boldsymbol{\psi})$ is a bias vector, and $\boldsymbol{\tau}$ is the generalized force vector. \mathbf{M}_* , \mathbf{b}_* and $\boldsymbol{\tau}_*$ are a block element or vector corresponding to the base-link, rigid-link or soft-segment part. Note that the upper part in $\boldsymbol{\tau}$ corresponding to the base-link is zero because the base-link is not fixed to the environment. Also, $\boldsymbol{\psi}$ is obtained from direct time-derivative of \mathbf{q} . For example, \mathbf{M}_0 is the inertia corresponding to $\dot{\boldsymbol{\eta}}_0$.

$\mathbf{J}_{C,i}$ is the Jacobian matrix of a contact point. We can calculate the Jacobian matrix for an arbitrary point by a simple extension of the traditional algorithm in the rigid-link system, as presented in [18].

2.3. Inverse Kinematics and Inverse Dynamics of Hybrid-link System

2.3.1. Inverse Kinematics for Motion Capture

The outline of inverse kinematics (IK) calculation to obtain the generalized coordinates of the hybrid-link system is summarized as follows. Let \mathbf{p}_i ($i = 1, \dots, M$) denote the

position vector of one of the total M markers in an optical motion capture system. We define a vector \mathbf{p} that concatenates these position vectors as

$$\mathbf{p} = [\mathbf{p}_1^T \quad \cdots \quad \mathbf{p}_M^T]^T. \quad (31)$$

In general, the IK computation is formulated as an optimization problem:

$$\min_{\mathbf{q}} \frac{1}{2} \|\widehat{\mathbf{p}} - \mathbf{p}(\mathbf{q})\|_{\mathbf{W}_1}^2 + \frac{1}{2} \|\mathbf{q}\|_{\mathbf{W}_2}^2, \quad (32)$$

where $\widehat{\mathbf{p}}$ is a measured value by the motion capture system, and $\mathbf{p}(\mathbf{q})$ is the marker position vector calculated in the hybrid-link model. The second term is a damping factor to suppress numerical instability due to a singular configuration, which is based on the Levenberg-Marquardt method.

2.3.2. Inverse Dynamics by Quadratic Programming

Inverse dynamics (ID) is utilized for estimating joint torques in a musculo-skeletal model [2,3] for a measured motion data. This calculation can be easily implemented in the hybrid-link system because of the similarity of the dynamics Eq. (29) with the traditional rigid-link system. In the case of the floating-base system, quadratic programming (QP) is often used for simultaneously calculating the joint torques and contact forces under its constraints.

We assume that time-series data of \mathbf{q} is obtained by the IK of the hybrid-link system, and its velocity $\dot{\boldsymbol{\psi}}$ and acceleration $\ddot{\boldsymbol{\psi}}$ as well. The ID calculates $\boldsymbol{\tau}_R, \boldsymbol{\tau}_S$ and $\mathbf{f}_{C,i}$ from the hybrid-link dynamics Eq. (29). We define vectors \mathbf{x} and \mathbf{f}_C that concatenate these variables as

$$\mathbf{x} := [\boldsymbol{\tau}_R^T \quad \boldsymbol{\tau}_S^T \quad \mathbf{f}_C^T]^T, \quad (33)$$

$$\mathbf{f}_C := [\mathbf{f}_{C,1}^T \quad \cdots \quad \mathbf{f}_{C,n_c}^T]^T \quad (34)$$

where n_c is the number of contact points. Given $\mathbf{q}, \dot{\boldsymbol{\psi}}$ and $\ddot{\boldsymbol{\psi}}$, we calculate the solution of \mathbf{x} by the following QP:

$$\min_{\mathbf{x}} \frac{1}{2} \|\mathbf{M}\dot{\boldsymbol{\psi}} + \mathbf{b} - \begin{bmatrix} \mathbf{0} \\ \boldsymbol{\tau}_R \\ \boldsymbol{\tau}_S \end{bmatrix} - \mathbf{J}_C^T \mathbf{f}_C\|_{\mathbf{W}_1}^2 + \frac{1}{2} \|\mathbf{x}\|_{\mathbf{W}_2}^2 \quad (35)$$

subject to

$$f_{C,i_z} > 0, \quad \sqrt{f_{C,i_x}^2 + f_{C,i_y}^2} \leq \mu f_{C,i_z},$$

where f_{C,i_x}, f_{C,i_y} and f_{C,i_z} are the elements of $\mathbf{f}_{C,i}$, and μ is the maximum static friction coefficient.

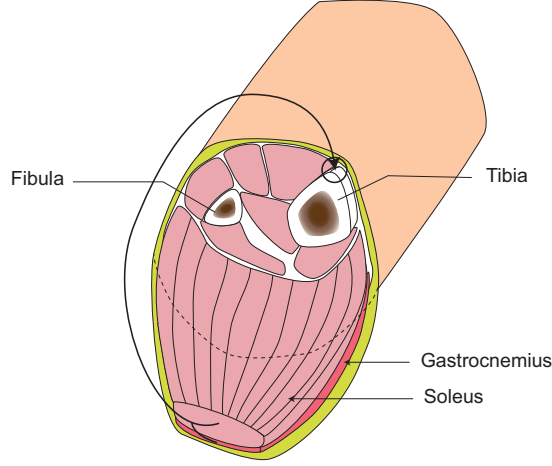


Figure 4. Schematics for the transtibial amputation surgery by myodesis focused on muscles

2.4. Muscle Force Estimation

2.4.1. Muscle Force Optimization

From the joint torques estimated by the ID, we can estimate muscle forces that actuate each joint. Because a human joint is redundantly actuated by multiple muscles, muscle forces \mathbf{f} are usually estimated by an optimization given as follows [2]:

$$\min_{\mathbf{f}} \frac{1}{2} \|\boldsymbol{\tau}_R - \mathbf{J}_\ell^T \mathbf{f}\|_{\mathbf{W}_1}^2 + \frac{1}{2} \|\mathbf{f} - \mathbf{f}_{ref}\|_{\mathbf{W}_2}^2 \quad (36)$$

subject to

$$\mathbf{0} \leq \mathbf{f} \leq \mathbf{f}_{\max} \quad (37)$$

where \mathbf{J}_ℓ is the Jacobian matrix of the muscle length, and \mathbf{f}_{\max} is the maximum muscle force calculated from Hill's model [20]. \mathbf{f}_{ref} is a reference value calculated from Hill's model as well if muscle activity can be obtained from electromyography (EMG) sensors.

2.4.2. Muscle Amputation Modeling

In this study, we use a musculo-skeletal model developed by [2] and modified it to consider a muscle amputation. It is known that there are two methods for amputation surgery: myodesis and myoplasty [21]. Myodesis is a method to drill a hole in a bone and secure muscles inside the hole whereas myoplasty stitches severed muscles over the end of the bone. Each method has advantages and limits, and a medical doctor chooses a method depending on various factors. Therefore, it is hard to unify the muscle model of amputation stump and need to design based on individual characteristic for accurate modeling.

In this study, we found that our subject had a myodesis surgery from MRI scanning of the subject and designed the amputation stump based on the observation. Fig. 4 illustrates the schematics for myodesis, focused on the muscle amputations, drawn based on [22]. The muscle amputation is summarized as follows:

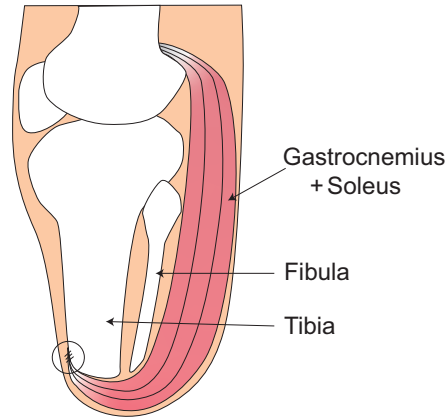


Figure 5. Schematic of the side view of the MRI scanning for leg with transtibial amputation operated by myodesis.



Figure 6. Arrangement of the transected muscles based on the MRI image of the subject.

- Anterior compartment musculature was removed.
- Deep posterior musculature (Gastrocnemius and Soleus) was transected and secured to the tibia via small holes.

If the transtibial amputation is operated by myodesis, the side view of the MRI scanning of the amputated leg can be illustrated as Fig. 5. Due to the personal information protection, we cannot include the actual MRI image in this paper. Instead, we observed that the gastrocnemius and the soleus shown in the MRI image had an arrangement similar to Fig. 5.

According to the aforementioned observation, we design the transected muscles as follows:

- Anterior compartment muscles (extensor digitorum longus, peroneus longus, plantaris, and tibialis anterior) are transected on the amputation stump and does not secured in any bone.
- Deep posterior musculature (Gastrocnemius and Soleus) was transected longer

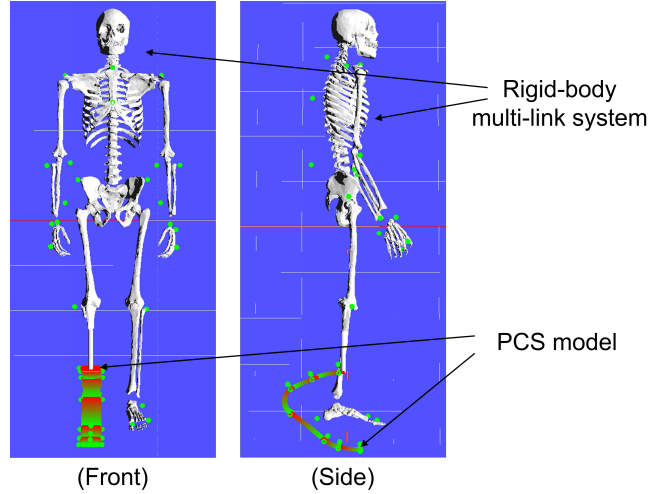


Figure 7. Hybrid-link model that integrates human skeleton and a leaf-spring prosthesis leg.

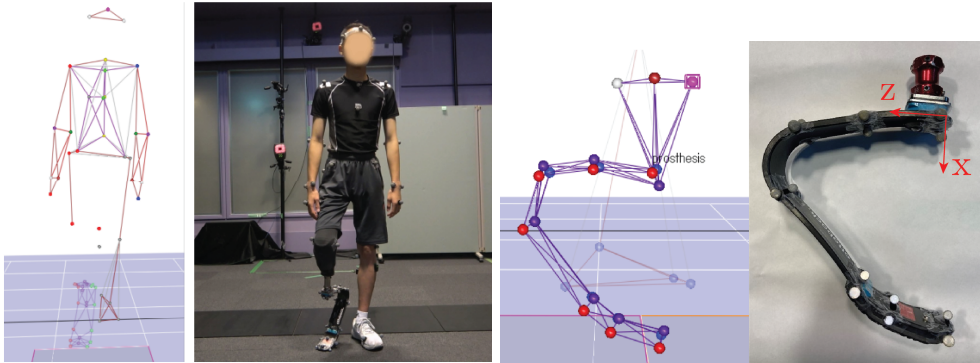


Figure 8. Layout of optical markers for motion capture measurement.

than the amputation stump. Also, the end of the muscles are secured to the front of the tibia. Therefore, these muscles has the shape as wrapping the tibia stump.

Fig. 6 shows the the muscle arrangement of an MRI-based designed amputation stump, in which each muscle is visualized as a simple thin wire without volume to show its arrangement. In this figure, the gastrocnemius and soleus muscles are wrapping tibia stump, as their endpoints are secured in the front of the tibia.

3. Experiments and Results

3.1. Motion Capture Measurement and Inverse Kinematics

We built a hybrid-link model for an athlete with a leaf-spring prosthesis leg, as shown in Fig. 7. The rigid part for the human skeletal model without right lower-limb is based on the musculoskeletal model developed in [2]. Different from [2], our model consists 50 rigid links and proper joints with 130 degrees of freedom (DOFs). A socket used to relate a severed human leg and prosthesis was designed as a rigid-link without DOF. The prosthetic leg (1E91 Runner by Ottobock) was designed as 6-segment PCS model.

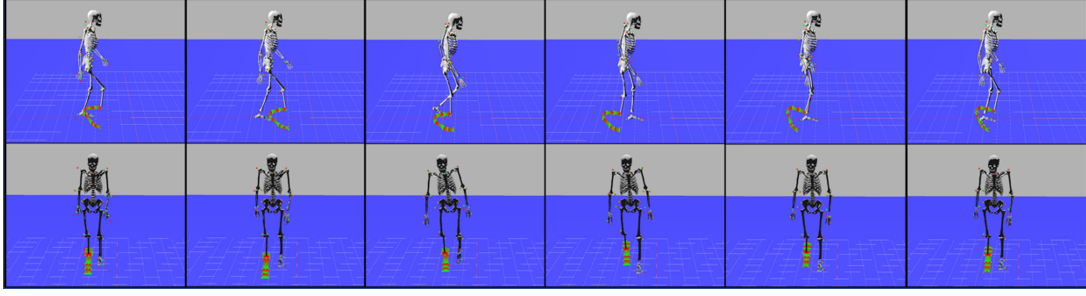


Figure 9. Walking motion reconstructed by the inverse kinematics of the hybrid-link system.

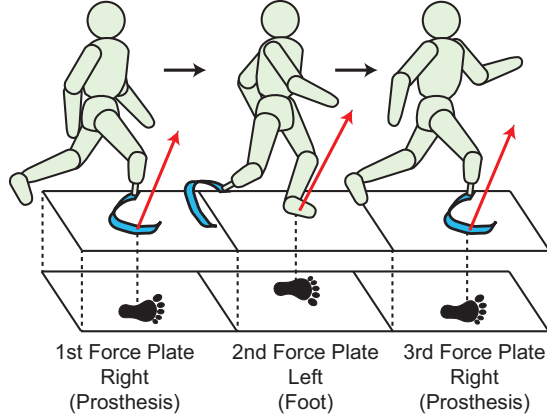


Figure 10. A subject was asked to walk or run with a single stride on each force plate in the experiment

The number of segments was determined based on the previous report [23], where the change ratio of strain along the central axis coordinate was large. We assume that each segment has only angular strain with 3 DOFs ignoring linear strain while $\mathbf{q}_{s,0}$ is calculated so that each segment has 6 DOFs for a precise modeling.

As a preliminary experiment [18], we obtained a walking motion of a subject wearing prosthesis. In the motion capture measurement, 51 optical markers were attached: 30 of them on human links and the remaining 21 on the prosthesis. Fig. 8 shows the layout of the markers. The subject was a healthy 15 year-old male who had undergone the right lower-extremity amputation approximately 13 cm from the knee. This subject wore a prosthesis on his right-side and walked on a treadmill with constant velocities 2.4km/h. The motion was captured with 200 Hz frequency.

Fig. 9 shows a walking motion reconstructed by the IK of the hybrid-link system. It is observed that the subject's motion is appropriately calculated by the IK.

3.2. Validation of Ground Reaction Force Estimation

We validate the ID calculation of the hybrid-link system using walking and running motions obtained from another motion capture measurement. While the experiment reported in Section 3.1 was on a treadmill, the subject was walking or running on three force plates in this experiment to measure the ground reaction force (GRF). As shown in Fig. 10, the subject was asked to walk or run with a single stride on each force plate. In the ID, we set candidates of the contact points: 6 points for the left foot and 4 points

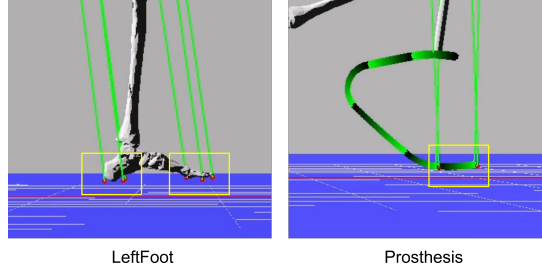


Figure 11. Setting of contact points in the inverse dynamics.

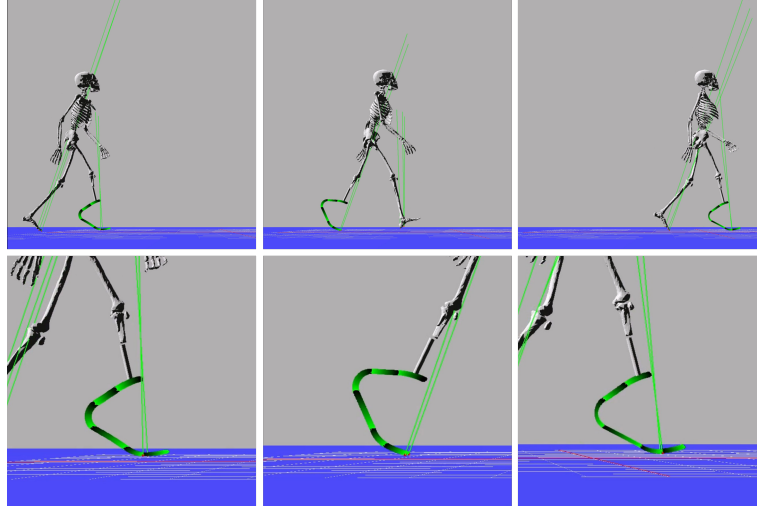


Figure 12. Reconstructed walking motion and estimated ground reaction force.

for the prosthesis, as shown in Fig. 11. Figs. 12 and 13 show reconstructed walking and running motions obtained from the experiment, respectively. In each figure, the green lines indicate the contact forces estimated by the ID calculation.

The ID estimates the joint torques of the human skeleton and generalized force of the prosthesis represented by the PCS model, in addition to the GRF. However, it is difficult to directly measure the first two values. Therefore, we validate the ID by comparing the estimated GRF with the ground truth obtained from the force plates. Figs. 14 and 15 show the results of the GRF estimation in the walking and running motions, respectively. In each figure, the blue and red lines indicate the ground truth and estimated values, respectively. Overall, it is observed that the estimated results are sufficiently close to the ground truth.

3.3. Comparison between Muscle Force Estimation by Optimization and that based on EMG Signal

Fig. 16 and accompanying video show a visualization of the estimated muscle activity, in which the red part indicates higher activity, and the green part indicates lower activity. For a quantitative verification, we compared the estimated muscle force by the optimization and the estimated value using the EMG signal (see Appendix A). For the comparison, we did not use the EMG signal in the optimization Eq. (36), setting

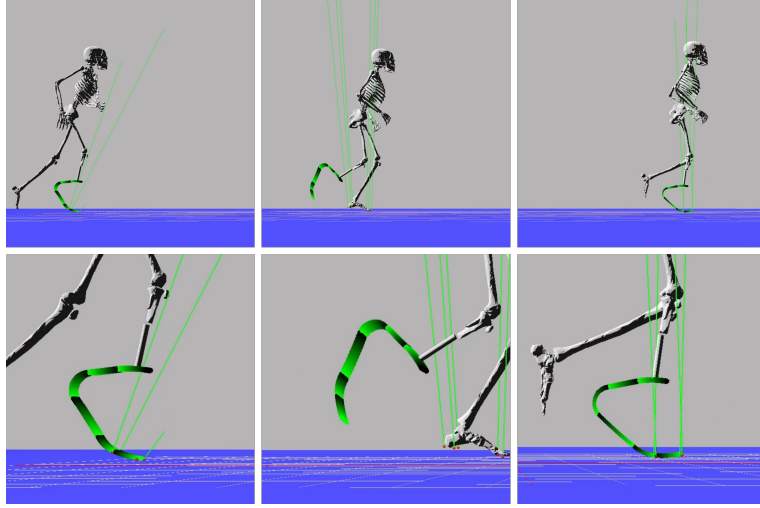


Figure 13. Reconstructed running motion and estimated ground reaction force.

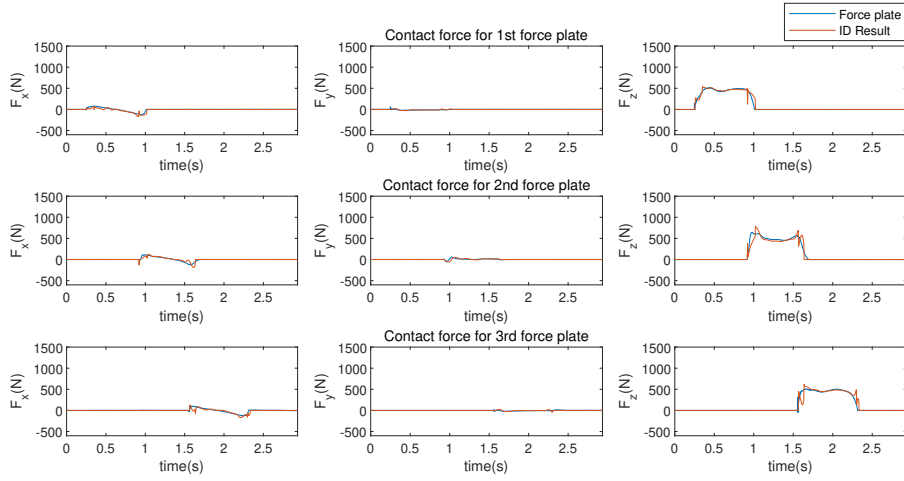


Figure 14. Estimated contact force and its ground truth along xyz axes in the walking motion.

$\mathbf{W}_2 = \mathbf{O}$. This would degrade the precision of the estimation; however, we excluded the EMG signal factor from the estimation for a pure comparison as a trial.

During the experiment, the subject wore tights to protect the connecting part between the socket and amputated leg. If the air enters inside the tights, the subject could not perform a running motion. Therefore, we need to attach EMG sensors without touching protection tights. From this reason, we attached two EMG sensors on the posterior leg, as shown in Fig. 17, which can be used to obtain a reliable result as possible. In Fig. 17, EMG sensor 1 is attached on the Semitendinosus, and EMG sensor 2 is attached on the biceps femoris caput longum muscle.

Ideally, we should compare the results of transected muscles to validate the model of amputation. However, it was hard to attach EMG sensors on the amputated muscles inside the protection tights due to the safety problem. Instead, we compared the results of biceps femoris caput longum muscle and semitendinosus muscle. Although these muscles are not transected ones, they also generate the knee joint torque, which

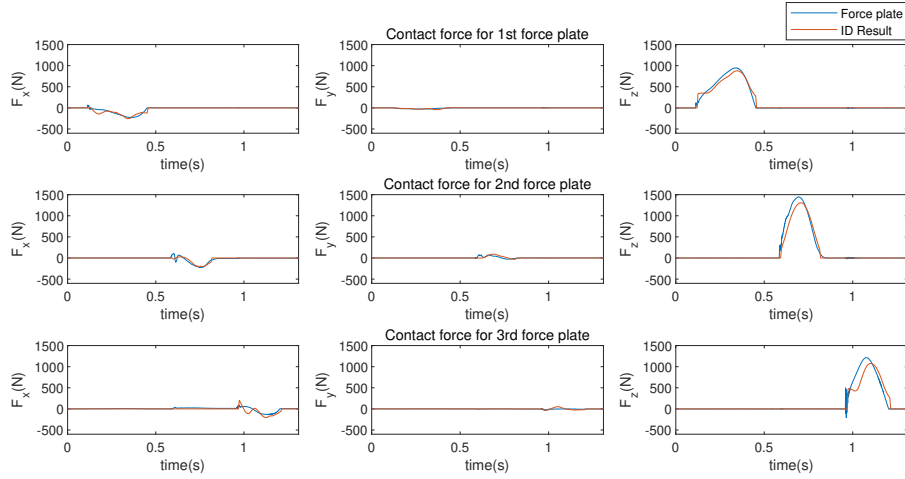


Figure 15. Estimated contact force and its ground truth along xyz axes in the running motion.

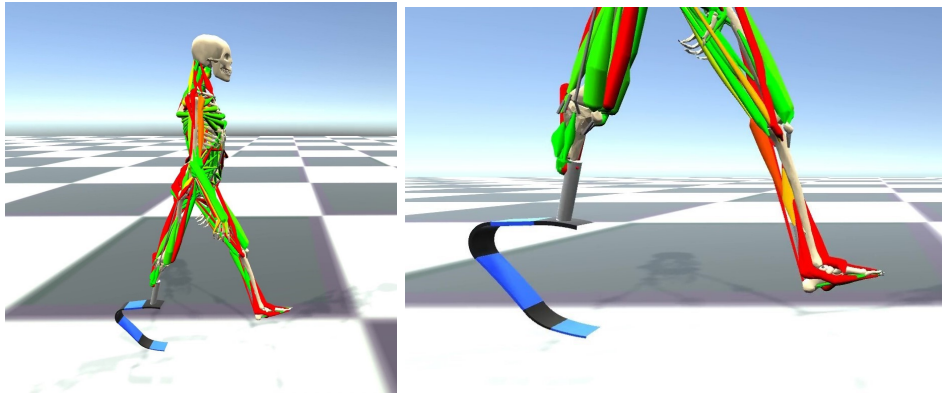


Figure 16. Visualization of estimated muscle activities, in which the red part indicates higher activity, and the green part indicates lower activity.

is the most affected joint from the transtibial muscle amputation. If the change of transected muscle tensions affects the knee joint torque, the action of these muscles will be altered together. Therefore, we consider that the evaluation of these two muscles is still reasonable.

Figs. 18 and 19 show the estimated muscle tension forces by optimization (indicated by the red line) and those by EMG signal (indicated by the blue line). In each figure, pink areas indicate the single phase with the right leg, in which the subject stood with the prosthesis on the force plate whereas green areas indicate the single phase with the left leg. Note that it is well-known that these two estimation does not have a precise agreement. Usually, it can be validated if a similar profile is obtained. In Figs. 18 and 19, we can observe a similarity between the two results in the first phase. In the second phase, a large portion of the optimization results is close to 0. In the third phase, it is observed that a larger muscle tension is estimated by the optimization than the EMG signal.

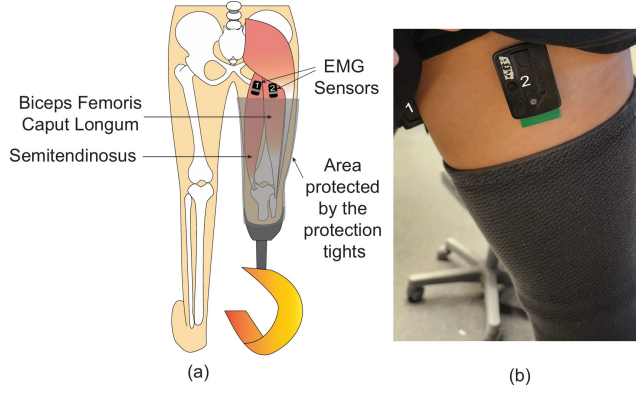


Figure 17. Location of the muscle and EMG sensors for the experiment

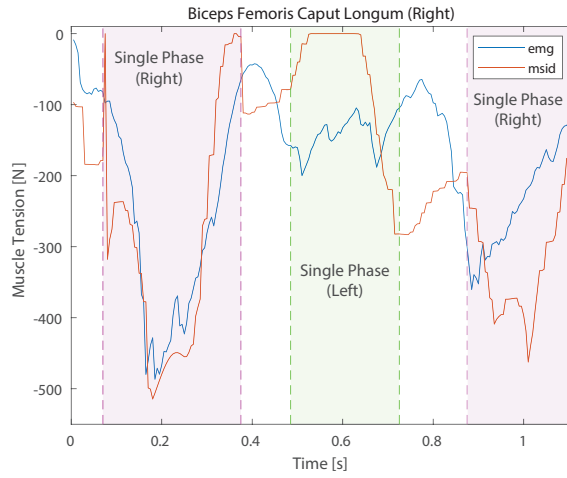


Figure 18. Muscle tension comparison between the estimations by the optimization and the EMG signal: Biceps Femoris Caput Longum

4. Discussions

4.1. Ground Reaction Force Estimation

Tables 1 and 2 show the root mean square error (RMSE) and related root mean square error (rRMSE) between the estimated and ground truth values, which are defined as follows [24]:

$$\text{RMSE} = \sqrt{\frac{\sum_{i=1}^n (f_i - \hat{f}_i)^2}{n}}, \text{ and} \quad (38)$$

$$\text{rRMSE} = \frac{\text{RMSE} \times 100}{1/2[\text{diff}(f_i) + \text{diff}(\hat{f}_i)]} \quad (39)$$

where n is the number of data, $\text{diff}(f) = \max(f) - \min(f)$, f is the GRF estimated from the ID, and \hat{f} is the ground truth measured by the force plate. These values were calculated only when the subject strode on each force plate.

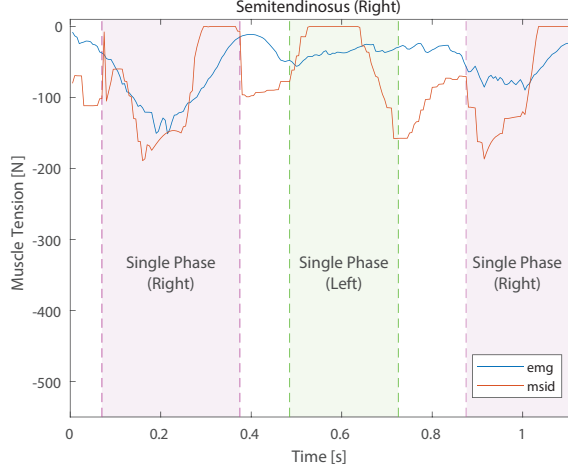


Figure 19. Muscle tension comparison between the estimations by the optimization and the EMG signal: Semitendinosus

Table 1. RMSE and rRMSE between estimated and measured contact force in the walking motion.

FP	x:RMSE(rRMSE)	y:RMSE(rRMSE)	z:RMSE(rRMSE)
1st	31.20N (11%)	8.67N (8%)	65.59N (9%)
2nd	37.81N (14%)	20.09N (18%)	107.39N (14%)
3rd	39.77N (14%)	11.58N (10%)	97.84N (13%)

- (1) Walking motion result: In Table 1, the rRMSE for the walking motion was approximately 12% in every axes. From Fig. 14, we observe that the error mainly occurs in the landing and pre-swing phases, when the foot or prosthesis is landing or departing from the ground. Meanwhile, stable results are observed in the mid-phases. We consider that one of the reasons is the limitation of the contact point setting. In the actual motion, the prosthesis has a rolling contact with the ground; however, it was simplified by a finite number of contacts as shown in Fig. 11.
- (2) Running motion result: As seen in Table 2, a relatively large rRMSE is observed compared to the walking motion, approximately 10% to 20% in every axes. Similar to the walking motion, the error largely occurs during the landing and pre-swing phases. However, in contrast to the walking motion, we found that there were fluctuations in the x- and y-axes of the estimated GRF. We consider that this is because the motion itself is faster than the walking motion, including a possibility that the motion data itself contains more noise.

Despite some limitations, the result of the ID is in good agreement with the measured ground truth with 12% rRMSE. These results show the validity of the ID calculation of the hybrid-link system.

Table 2. RMSE and rRMSE between estimated and measured contact force in the running motion.

FP	x:RMSE(rRMSE)	y:RMSE(rRMSE)	z:RMSE(rRMSE)
1st	48.50N (13%)	11.69N (10%)	96.75N (7%)
2nd	46.93N (12%)	33.95N (29%)	178.95N (12%)
3rd	76.63N (20%)	24.83N (21%)	222.23N (15%)

Table 3. Root Mean Square Error between the estimations by the optimization and the EMG signal for each single phase.

RMS Error[%]	1st (Right)	2nd (Left)	3rd (Right)
Biceps Femoris Caput Longum	7.4843	10.5783	10.4043
Semitendinosus	8.8415	10.4481	12.2633

4.2. Muscle Force Estimation

Table 3 shows the root mean square error between the two estimations, divided by $\max(f_{\max i})$ of each muscle. This result is calculated only for each single phase. We consider that there are mainly two reasons in the error. Firstly, there was a limitation on the position to attach the EMG sensors in this experiment. Usually, EMG sensor is attached on the middle of a muscle to obtain accurate result. We consider the location of EMG sensor attached near the end part would degrade the accuracy. Secondly, we consider that there was a limitation of the optimization method itself. In Figs. 18 and 19, continuous zero values are sometimes observed from the result. For a limitation of the muscle force optimization, the system cannot calculate the muscle force when the joint is in static movement such as the single support phase. Therefore, as a reason for zero values, we consider that the related joint was rarely moving in those moments. EMG signals are usually used for compensation of this problem, included in the optimization Eq. (36). Therefore, it is expected that a better estimation result will be obtained using EMG signal in the optimization.

Although there are limitations, Table 3 shows low values for RMSE, especially for the first stance phase with the prosthetic leg. From these results, we consider that the proposed musculoskeletal model with hybrid-link system can provide an estimation of muscle force, explicitly considering the deformation of the flexible prosthesis and muscle amputation.

Although we set $\mathbf{W}_2 = \mathbf{O}$ for comparison, appropriate setting of \mathbf{W}_2 would improve the estimation of muscle forces, using EMG signals as reference. This is one of our future works.

5. Conclusion

In this study, we introduced a framework for the dynamical analysis of an athlete motion wearing a leaf-spring prosthesis, based on the inverse dynamics of a soft-rigid hybrid multi-link system. The obtained results can be summarized as follows:

- (1) We built a hybrid-link model that integrated human skeleton system with a leaf-spring prosthesis, in which the flexible deformation of the prosthesis was represented by the PCS model developed in soft robotics research field. We implemented the inverse kinematics of the hybrid-link system and applied it to the motion reconstruction from the motion captured data.
- (2) Using the QP-based inverse dynamics, we can estimate the joint torques and ground reaction force during a motion, explicitly considering the interaction force between human limb and prosthesis leg. Comparing the rRMSE between the measured force and estimated force, the results showed that the error was low in the mid phase but high in the landing and pre-swing phases. Despite limitations, we showed that the rRMSE was approximately 12% in the walking motion.

- (3) We can estimate muscle tension force by the optimization using the result obtained from the inverse dynamics. We built a muscle model to replicate the muscle amputation and estimated the muscle force during a running motion. We quantitatively compared it with another estimation by EMG signals and showed that the RMSE between two values shows around 10% error for the maximum muscle tension.

A known limitation in this study is that all results were made for only one subject. This was because it was hard to find a subject who wears a leaf-spring prosthesis playing sports and can participate in an experiment. Future experiments with much more subjects will provide more reliable results. We believe that this study contributes to an important step for biomechanical analysis in Para-sport field as a practical application of the traditional robotics and latest soft robotics research.

Appendix A. Muscle Tension Force Calculation using EMG Signal

In muscle model proposed by Hill [20], the muscle is modeled by using the muscle length and velocity. To complement the intrinsic muscle stiffness which is not properly represented in Hill-type muscle model, Stroeve [25] proposed neuro-musculo-skeletal model, using the muscle model as a simplification of [26]. According to [25], an arbitrary muscle tension force f_i is given by

$$f_i = -a_i F_l(l_i) F_v(\dot{l}_i) F_{\max i} \quad (\text{A1})$$

where a_i is muscle activity; l_i and \dot{l}_i are muscle length and velocity, respectively; $F_{\max i}$ is maximum isometric force of muscle i ; $F_l(l_i)$ is Gaussian force-length relation; and $F_v(\dot{l}_i)$ is Hill-type force-velocity relation.

Muscle activity at current state $a_i(t)$ is updated from the EMG signal as follows:

$$\dot{a}_i(t) = \frac{u_i - a_i(t-1)}{\tau^*} \quad (\text{A2})$$

$$\tau^* = \begin{cases} \tau_{ac} & u_i \geq a_i(t-1) \\ \tau_{da} & u_i < a_i(t-1) \end{cases} \quad (\text{A3})$$

$$u_i = \frac{u_{\text{EMG}}}{u_{\text{MVC}}} \quad (\text{A4})$$

where τ_{ac} is an activation time constant; τ_{da} is a deactivation time constant; and u_i is the neural input obtained from EMG signal u_{EMG} and Maximum Voluntary Contraction (MVC) of corresponding muscle u_{MVC} . Finally, we can compute the muscle tension f_i from the EMG signal.

Appendix B. Inertia Matrix of Hybrid-link System

The inertia matrix $\mathbf{M}(\mathbf{q})$ in Eq. (29) or (30) can be derived in a manner similar to that of a rigid-body multi-link system. First, the kinetic energy of a single rigid-link

is represented as

$$T_{R,i} = \frac{1}{2} \boldsymbol{\eta}_i^T \mathcal{M}_{R,i} \boldsymbol{\eta}_i, \quad (\text{B1})$$

$$\mathcal{M}_{R,i} := \begin{bmatrix} \mathbf{I}_{G,i} & \mathbf{O} \\ \mathbf{O} & m_i \mathbf{E} \end{bmatrix} \quad (\text{B2})$$

where $\mathbf{I}_{G,i}$ is the 3×3 inertia matrix about the center of gravity of a rigid link. Then, $T_{R,i}$ can be rewritten as

$$T_{R,i} = \frac{1}{2} \boldsymbol{\psi}^T \mathbf{J}_{R,i}^T \mathcal{M}_{R,i} \mathbf{J}_{R,i} \boldsymbol{\psi} \quad (\text{B3})$$

using $\boldsymbol{\eta}_i = \mathbf{J}_{R,i} \boldsymbol{\psi}$ with the Jacobian matrix $\mathbf{J}_{R,i}$.

Then, the kinetic energy of a segment in the PCS model can be represented by the same formulation as

$$T_{S,i} = \frac{1}{2} \boldsymbol{\psi}^T \mathbf{J}_{S,i}^T \mathcal{M}_{S,i} \mathbf{J}_{S,i} \boldsymbol{\psi} \quad (\text{B4})$$

because of the similarity of the mathematical structure between the rigid-body and PCS model although the detailed contents of $\mathcal{M}_{S,i}$ is more complicated than $\mathcal{M}_{R,i}$.

From Eqs. (B3) and (B4), the total kinetic energy of a hybrid-link system can be represented as

$$T = \sum_i T_{R,i} + \sum_i T_{S,i} = \frac{1}{2} \boldsymbol{\psi}^T \left(\sum_i \mathbf{J}_{R,i}^T \mathcal{M}_{R,i} \mathbf{J}_{R,i} + \sum_i \mathbf{J}_{S,i}^T \mathcal{M}_{S,i} \mathbf{J}_{S,i} \right) \boldsymbol{\psi} \quad (\text{B5})$$

Therefore, the total inertia matrix of $\mathbf{M}(\mathbf{q})$ is derived as

$$\mathbf{M}(\mathbf{q}) = \sum_i \mathbf{J}_{R,i}^T \mathcal{M}_{R,i} \mathbf{J}_{R,i} + \sum_i \mathbf{J}_{S,i}^T \mathcal{M}_{S,i} \mathbf{J}_{S,i} \quad (\text{B6})$$

Each block in $\mathbf{M}(\mathbf{q})$ such as \mathbf{M}_0 and \mathbf{M}_{R0} is derived from Eq. (B6). In practice, however, it is more efficient to numerically compute than to analytically calculate those matrices, e.g., by the unit vector method. Or, the articulated body algorithm, which has been proposed also for the PCS model [14], does not explicitly compute those matrices but directly compute the acceleration.

Acknowledgements

The experiment of this research was conducted thanks to the cooperation of Dr. Sayaka Fujiwara, the Faculty of Medicine, University of Tokyo. The authors also thank Yosuke Ikegami and Kazuya Tomabechei for their advise on the musculo-skeletal model and motion capture measurement, Kensho Hiraoka for his support for the motion capture measurement, and Akihiro Sakurai for his support for the visualization of muscle activities.

Disclosure statement

No potential conflict of interest was reported by the authors.

Funding

This work was supported by JSPS KAKENHI 21H01282.

References

- [1] Hobara H, Kobayashi Y, Heldoorn TA, et al. The fastest sprinter in 2068 has an artificial limb? ; 2015.
- [2] Nakamura Y, Yamane K, Fujita Y, et al. Somatosensory computation for man-machine interface from motion-capture data and musculoskeletal human model. *IEEE Transactions on Robotics*. 2005;21(1):58–66.
- [3] Delp SL, Anderson FC, Arnold AS, et al. Opensim: open-source software to create and analyze dynamic simulations of movement. *IEEE transactions on biomedical engineering*. 2007;54(11):1940–1950.
- [4] Rigney SM, Simmons A, Kark L. A prosthesis-specific multi-link segment model of lower-limb amputee sprinting. *Journal of Biomechanics*. 2016;49(14):3185–3193.
- [5] Kleesattel ALEN, Mombaur K. Inverse optimal control based enhancement of sprinting motion analysis with and without running-specific prostheses. In: 2018 7th IEEE International Conference on Biomedical Robotics and Biomechatronics (Biorob); IEEE; 2018. p. 556–562.
- [6] Murai A, Hobara H, Hashizume S, et al. Can forward dynamics simulation with simple model estimate complex phenomena?: Case study on sprinting using running-specific prosthesis. *Robomech Journal*. 2018;5(1):1–8.
- [7] Duriez C. Control of elastic soft robots based on real-time finite element method. In: 2013 IEEE international conference on robotics and automation; IEEE; 2013. p. 3982–3987.
- [8] Mendhurwar K, Handa G, Zhu L, et al. A system for acquisition and modelling of ice-hockey stick shape deformation from player shot videos. In: Proceedings of the IEEE/CVF Conference on Computer Vision and Pattern Recognition Workshops; 2020. p. 890–891.
- [9] Kays BT, Smith LV. Effect of ice hockey stick stiffness on performance. *Sports Engineering*. 2017;20:245–254.
- [10] Vivaldi F, Cortese L, Coppola T, et al. A study on the dynamic structural behavior of olympic sabres. *Procedia Structural Integrity*. 2018;8:345–353.
- [11] Runge G, Raatz A. A framework for the automated design and modelling of soft robotic systems. *CIRP Annals*. 2017;66(1):9–12.
- [12] Schegg P, Duriez C. Review on generic methods for mechanical modeling, simulation and control of soft robots. *Plos one*. 2022;17(1):e0251059.
- [13] Antman SS. *Nonlinear problems of elasticity*. New York: Springer; 2005.
- [14] Renda F, Boyer F, Dias J, et al. Discrete cosserat approach for multisection soft manipulator dynamics. *IEEE Transactions on Robotics*. 2018;34(6):1518–1533.
- [15] Renda F, Seneviratne L. A geometric and unified approach for modeling soft-rigid multi-body systems with lumped and distributed degrees of freedom. In: 2018 IEEE International Conference on Robotics and Automation (ICRA); IEEE; 2018. p. 1567–1574.
- [16] Ishigaki T, Yamamoto K. Dynamics computation of a hybrid multi-link humanoid robot integrating rigid and soft bodies. In: 2021 IEEE/RSJ International Conference on Intelligent Robots and Systems (IROS); IEEE; 2021. p. 2816–2821.
- [17] Mathew AT, Hmida IB, Armanini C, et al. Sorosim: A matlab toolbox for hybrid rigid-soft

- robots based on the geometric variable-strain approach. *IEEE Robotics and Automation Magazine*. 2023 9;30:106–122.
- [18] Kim S, Ishigaki T, Shimane Y, et al. Inverse kinematics of hybrid multi-link system and its application to motion capture for athlete wearing sports prosthesis. In: 2022 IEEE-RAS 21st International Conference on Humanoid Robots (Humanoids); IEEE; 2022. p. 837–842.
 - [19] Featherstone R. Rigid body dynamics algorithms. Springer; 2008.
 - [20] Hill AV. The heat of shortening and the dynamic constants of muscle. *Proceedings of the Royal Society of London Series B-Biological Sciences*. 1938;126(843):136–195.
 - [21] Geertzen JH, van der Schans SM, Jutte PC, et al. Myodesis or myoplasty in trans-femoral amputations. what is the best option? an explorative study. *Medical Hypotheses*. 2019; 124:7–12.
 - [22] Brown BJ, Iorio ML, Klement M, et al. Outcomes after 294 transtibial amputations with the posterior myocutaneous flap. *The international journal of lower extremity wounds*. 2014;13(1):33–40.
 - [23] Shimane Y, Ishigaki T, Kim S, et al. Application of piece-wise constant strain model to flexible deformation calculation of sports prosthesis and stiffness estimation. In: 2022 IEEE Int. Conf. Intell. Robots Syst.; (To be published).
 - [24] Oh SE, Choi A, Mun JH. Prediction of ground reaction forces during gait based on kinematics and a neural network model. *Journal of biomechanics*. 2013;46(14):2372–2380.
 - [25] Stroeve S. Impedance characteristics of a neuromusculoskeletal model of the human arm i. posture control. *Biological cybernetics*. 1999;81(5-6):475–494.
 - [26] Winters JM, Stark L. Analysis of fundamental human movement patterns through the use of in-depth antagonistic muscle models. *IEEE transactions on biomedical engineering*. 1985;(10):826–839.